

PCH-2^{TRIP13} regulates spindle checkpoint strength

Lénaïg Défachelles, Anna E. Russo, Christian R. Nelson and Needhi Bhalla*

Department of Molecular, Cell and Developmental Biology, University of California,

Santa Cruz,

Santa Cruz, CA 95064

*corresponding author: nbhalla@ucsc.edu

Department of Molecular, Cell and Developmental Biology

225 Sinsheimer Labs

University of California, Santa Cruz

Santa Cruz, CA 95064

phone: (831) 459-1319

fax: (831) 459-3139

Key words: *C. elegans*, mitosis, embryo, spindle assembly checkpoint, Mad2,

aneuploidy, germline

ABSTRACT

Spindle checkpoint strength, defined as the length of the cell cycle delay imposed by the spindle checkpoint, is dictated by three criteria: the number of unattached kinetochores, cell volume and cell fate. However, how checkpoint strength is regulated is unknown. We show that the conserved AAA-ATPase, PCH-2, which remodels the essential checkpoint effector Mad2 from an active conformation to an inactive one, controls checkpoint strength in *C. elegans*. When we genetically manipulate embryos to decrease cell volume, PCH-2 is no longer required for the spindle checkpoint or recruitment of Mad2 at unattached kinetochores, showing that PCH-2 is essential for a robust checkpoint in large cells. This role in checkpoint strength is not limited to large cells: germline precursor cells exhibit a stronger checkpoint than their somatic counterparts and this also relies on PCH-2. PCH-2 is more highly enriched in germline precursor cells than in somatic cells and this enrichment relies on a conserved factor that induces asymmetry in the early embryo. Finally, the stronger checkpoint in germline precursor cells also depends on CMT-1, which is essential for both PCH-2's localization to unattached kinetochores and its enrichment in germline precursor cells. Thus, PCH-2's ability to regulate the availability of an inactive but necessary checkpoint precursor at or near unattached kinetochores governs checkpoint strength.

INTRODUCTION

To prevent the missegregation of chromosomes and the production of daughter cells with an incorrect number of chromosomes, the spindle checkpoint (also called the spindle assembly checkpoint) monitors whether chromosomes are attached to the spindle via kinetochores. If kinetochores fail to attach properly, this checkpoint delays the cell cycle to promote error correction and prevent aneuploidy. Despite its critical role, the strength of the spindle checkpoint, defined as the duration of the cell cycle delay, can be highly variable. This variability is controlled by the number of unattached kinetochores (Collin et al., 2013), cell volume, (Kyogoku and Kitajima, 2017; Galli and Morgan, 2016) and cell fate (Galli and Morgan, 2016; Gerhold et al., 2018).

The spindle checkpoint response initiates with the recruitment of Mad1 and Mad2 at unattached kinetochores (Sironi et al., 2001), which catalyzes the production of a Mitotic Checkpoint Complex (MCC) (Chen et al., 1996; Li and Benezra, 1996; Chen et al., 1998). The MCC enforces a checkpoint arrest by inhibiting the Anaphase Promoting Complex/Cyclosome (APC/C) and preventing cell cycle progression (Sudakin et al., 2001). Formation of the MCC is driven by conformational changes in Mad2, which can exist in an open conformation (O-Mad2) or a closed conformation (C-Mad2) (Luo et al., 2002; Sironi et al., 2002; Luo et al., 2004). Mad2 is in the closed conformation in the Mad1/Mad2 tetramer recruited to unattached kinetochores. C-Mad2 in the tetramer acts as a template to convert additional soluble O-Mad2 to C-Mad2, which can be assembled into the MCC (Sironi et al., 2001; De Antoni et al., 2005; Fava et al., 2011). Thus, unattached kinetochores act as a platform for MCC assembly. The MCC effectively tunes the spindle checkpoint response: the length of the cell cycle delay imposed by the

checkpoint is governed by the ratio of the soluble MCC checkpoint signal to cytoplasmic volume (Collin et al., 2013; Dick and Gerlich, 2013).

PCH-2, known as TRIP13 in mammals, is a hexameric AAA+ ATPase that remodels HORMA domain-containing proteins, a group that includes Mad2 (Aravind and Koonin, 1998; Chen et al., 2014; Vader, 2015; Ye et al., 2015). Originally described as a spindle checkpoint silencing protein, experiments showed that TRIP13 works with the adaptor protein p31^{comet} to extract C-Mad2 from the MCC and promote its disassembly, permitting the activation of the APC/C (Wang et al., 2014; Eytan et al., 2014; Ye et al., 2015; Miniowitz-Shemtov et al., 2015; Brulotte et al., 2017; Alfieri et al., 2018). We and others have shown that PCH-2/TRIP13 is essential for spindle checkpoint activation in *C. elegans* and mammalian cells (Nelson et al., 2015; Ma and Poon, 2016; Yost et al., 2017). PCH-2 is present at unattached kinetochores (Tipton et al., 2012; Wang et al., 2014; Nelson et al., 2015) and is required to robustly localize Mad2, but not Mad1, to unattached kinetochores (Nelson et al., 2015; Yost et al., 2017). Biochemical and structural studies have shown that PCH-2 converts C-Mad2 to O-Mad2 (Ye et al., 2015; Brulotte et al., 2017; Alfieri et al., 2018). Altogether, these data suggest a model in which PCH-2 converts a population of C-Mad2 that is not competent for checkpoint signaling into O-Mad2, so that Mad1/Mad2 recruited to unattached kinetochores can template C-Mad2 for assembly into the MCC.

This model has major implications for our understanding of the spindle checkpoint. First, it indicates that the spindle checkpoint does not simply depend on the presence of C-Mad2. Rather, only C-Mad2 that has been assembled into the MCC at unattached kinetochores is competent for checkpoint signaling (Ma and Poon, 2016). Second, it suggests that there is a significant population of C-Mad2 in cells that must be liberated

for a functional checkpoint. In *C. elegans*, some of this C-Mad2 appears to be complexed with and stabilized by the Mad2 mimic p31^{comet} (CMT-1 in *C. elegans*) (Yang et al., 2007; Nelson et al., 2015); loss of CMT-1 partially suppresses the spindle checkpoint defect in *pch-2* mutants, likely by liberating enough O-Mad2 to make PCH-2 partially dispensable (Nelson et al., 2015). In cells that have a significant population of available O-Mad2, such as HeLa cells (Luo et al., 2004), TRIP13 function becomes essential for checkpoint activity only when this population of O-Mad2 is limiting (Ma and Poon, 2018).

Here, we show that PCH-2's role in regulating the availability of O-Mad2 controls spindle checkpoint strength in *C. elegans*. Despite being essential for the spindle checkpoint in the large somatic, or AB, cell of the two-cell embryo, PCH-2 becomes dispensable as AB cells are genetically manipulated to become smaller, suggesting that PCH-2's ability to concentrate O-Mad2 near unattached kinetochores is essential for checkpoint activation in large cells. Indeed, as AB cells become smaller PCH-2 is also dispensable for Mad2 recruitment at unattached kinetochores. This requirement in promoting spindle checkpoint strength is also observed in germline precursor, or P₁, cells, which have a stronger checkpoint than their somatic counterparts. PCH-2 is enriched in P₁ cells and this enrichment is dependent on a conserved regulator of embryonic polarity, PAR-1. Further, the stronger checkpoint in P₁ cells also relies on the *C. elegans* ortholog of p31^{comet}, CMT-1, suggesting that CMT-1's role in localizing PCH-2 to unattached kinetochores and/or its ability to enrich PCH-2 in P₁ cells, contributes to a stronger checkpoint. We propose that in scenarios where maintaining genomic stability can be particularly challenging and/or relevant, such as in oocytes and early embryos enlarged for developmental competence and germline cells that maintain immortality, PCH-2, and

its mammalian ortholog TRIP13, ensure a robust spindle checkpoint response and proper chromosome segregation.

MATERIALS AND METHODS

Worms strains

The *C. elegans* Bristol N2 (Brenner, 1974) was used as the wild-type strain. All strains were maintained at 20°C. See Table S1 for the list of all the strains used in this study.

Immunostaining

Immunostaining was performed on adult worms 48h after L4, as described in (Bhalla and Dernburg, 2005). The antibodies used were rabbit anti-MAD-2 (1/500; Essex et al., 2009) and mouse anti-MAb414 (1/400; Davis and Blobel, 1986). Secondary antibodies were Alexa Fluor 488 anti-rabbit (Invitrogen) and Cy3 anti-mouse (Jackson ImmunoResearch Laboratories, Inc.) diluted at 1:500. Antibody against MAD-2 was a gift from A. Desai (Ludwig Institute/University of California, San Diego, La Jolla, CA).

Images were acquired on a DeltaVision Personal DV microscope (GE Healthcare) equipped with a 100× NA 1.40 oil-immersion objective (Olympus), a short ARC xenon lamp (GE Healthcare) and using a CoolSNAP charge-coupled camera (Roper Scientific). Z-stacks were collected at 0.2 μm Z-spacing and processed by constrained, iterative deconvolution. Imaging, image scaling, and analysis were performed using functions in the softWoRx software package (GE Healthcare). Projections were calculated by a maximum intensity algorithm. Composite images were assembled and some false coloring was performed with Fiji.

Live imaging of two-cell embryos

For live imaging of two-cell embryos, worms were dissected on glass coverslips in egg buffer and then mounted on 2% agar pads. Images were acquired every 1 minute or 20 seconds on a DeltaVision Personal DV microscope as described in the previous section; except that the distance between two planes was 2 μm . The mitotic timing was measured from NEBD to OCC as described in (Nelson et al., 2015). Cell volumes were measured as described in (Galli and Morgan, 2016). To measure the nuclear area, a sum projection of the embryo was generated 1 minute before chromosomes began to condense and the area was measured with Fiji (Figure S2A).

Live imaging of embryogenesis

After a treatment with *perm-1^{RNAi}* (see below), worms were dissected onto a coverslip with egg salt buffer (118 mM NaCl, 48 mM KCl) supplemented with 10 mM PIPES pH 7.3, 1 mM ATP and 10 mM sucrose. Embryos and adult carcasses were transferred into a well of an 8-well plate (ibidi 1 μ -Slide 8 Well Glass bottom) that had been freshly coated with 0.1% Poly-L-Lysine solution (Sigma P8920) and extensively washed. Time-lapse videos were acquired with a Solamere spinning disk confocal system piloted by μ Manager software (Edelstein et al., 2014) and equipped with a Yokogawa CSUX-1 scan head, a Nikon (Garden City, NY) TE2000-E inverted stand, a Hamamatsu ImageEM $\times 2$ camera, LX/MAS 489 nm and LS/MAS 561 nm laser, and Plan Apo $\times 60/1.4$ numerical aperture oil objective. Acquisition times per frame were 50 ms using 5% of the lasers power for both channels, and images were obtained as stacks of planes at 2 μm intervals taken every 1 minute. Nocodazole was added from a 5X stock to a final concentration of 50 μM after the first time point.

Quantification of fluorescence intensity

To quantify GFP::MAD-2 and PCH-2::GFP levels, images were generated under the same conditions as previously described for the live imaging of two-cell embryos with a few modifications: only the nucleus was imaged, the interval between two planes was 1 μm and images were collected every 20 seconds. To measure the cell volume, one Z-stack of the entire cell was taken at NEBD at 2 μm Z-spacing. Quantification of fluorescence at kinetochores or around mitotic chromosomes was performed in Fiji as described in (Moyle et al., 2014; Nelson et al., 2015) and fluorescence in the cytoplasm as describes in (Galli and Morgan, 2016).

Feeding RNAi

C. elegans strains were fed HT115 bacteria expressing the desired dsRNA after IPTG induction. Bacterial strains containing RNAi vectors were cultured overnight at 37°C, centrifuged, and the pellet was resuspended in 1/50 of the original volume. 100 μl of concentrated culture was spotted onto a nematode growth medium (NGM) plate containing 1 mM IPTG and 50 $\mu\text{g}/\mu\text{l}$ of kanamycin or carbenicillin and the plate was incubated overnight at 37°C.

For *ani-2^{RNAi}*, gravid adults were bleached onto the RNAi plate and their progeny was allowed to develop at 20°C during 2.5 days. Then, L4s were transferred to a fresh plate containing OP50 or *zyg-1^{RNAi}* bacteria.

For *zyg-1^{RNAi}*, L4s were transferred (from an OP50 or *ani-2^{RNAi}* plate) onto a *zyg-1^{RNAi}* plate and cultured 1.5 days at 20°C.

For *perm-1^{RNAi}*, young adults (8h post L4) were incubated onto *perm-1^{RNAi}* plates for 16-20h at 15°C.

200

201 For *par-1^{RNAi}*, gravid adults were bleached onto control RNAi (L4440) plates and their
202 progeny were allowed to develop at 15°C for 3 days. L4s were then transferred onto *par-*
203 *1^{RNAi}* or control RNAi (L4440) plates and incubated at 15°C for 3 days.

204

205 **Statistical Analysis**

206 Linear regression analysis and assessing significance of this data (Figures 1C, 4A, 4B,
207 S1B, S1D) was performed using GraphPad Prism version 6 for Macintosh. For all other
208 data, significance was assessed by performing t-tests (Figures 1D, 2C, 3, 4C, 5A, 5C,
209 5D, 6A, 6C, 6D, S3B, S3D, and S4B). In all graphs, a * indicates a p value < 0.05, **
210 indicates a p value < 0.01 and *** a p value < 0.0001.

211

212 **RESULTS**

213

214 **PCH-2 becomes dispensable for the spindle checkpoint response in somatic cells** 215 **as they decrease in size**

216 In the large somatic, or AB, cell of the *C. elegans* two-cell embryo, PCH-2 is essential for
217 spindle checkpoint activation (Nelson et al., 2015). To further assess the requirements
218 for PCH-2 function, we manipulated the cell volume of AB cells experimentally by
219 performing RNA interference (RNAi) against *ani-2*. *ani-2* encodes a germline specific
220 anillin whose depletion generates oocytes and, after fertilization, embryos, of varying
221 size (Maddox et al., 2005) (Figure 1A). We monitored the length of mitosis in these
222 embryos, using the time between nuclear envelope breakdown (NEBD) to the onset of
223 cortical contractility (OCC) as markers for the entry into and exit from mitosis,
224 respectively (Essex et al., 2009). We then correlated the length of mitosis to cytoplasmic
225 volume. RNAi of *ani-2* did not affect cell cycle progression in control, *pch-2*, or *mad-1*

mutants (Figure S1A), indicating that reducing cytoplasmic volume did not affect mitotic timing in these embryos.

We performed double depletion of *ani-2* and *zyg-1* to induce the spindle checkpoint response in control embryos, *pch-2*, and *mad-1* mutants. ZYG-1 is essential for centrosome duplication after the first embryonic division, its depletion generates monopolar spindles (O'Connell et al., 2001) and unattached kinetochores (Essex et al., 2009) (Figure 1B). Consistent with previous reports, as cells decreased in cell volume the length of the cell cycle delay, an indicator of spindle checkpoint strength, increased in control embryos (Galli and Morgan, 2016; Gerhold et al., 2018) (Figure 1C). Surprisingly, as *pch-2* mutant embryos decreased in size, the spindle checkpoint response more closely resembled that of similarly sized control embryos than similarly sized *mad-1* mutant embryos (Figure 1C). There was no significant difference between the slopes of the regression analysis of control and *pch-2* mutant data (p value = 0.1407), while the slopes between the regression analysis of *pch-2* and *mad-1* mutant data were significantly different (p value = 0.0007). We binned our data and observed that *pch-2* mutant embryos fell into three clear categories: 1) wild-type sized embryos (more than $5 \times 10^3 \mu\text{m}^3$) in which PCH-2 was essential for the spindle checkpoint; 2) medium sized embryos (between $3.5 \times 10^3 \mu\text{m}^3$ and $5 \times 10^3 \mu\text{m}^3$), which exhibited an intermediate level of checkpoint function; and 3) small embryos (less than $3.5 \times 10^3 \mu\text{m}^3$), in which PCH-2 was completely dispensable for the spindle checkpoint response (Figure 1D).

We verified that the mitotic delay observed in *pch-2* embryos was a legitimate spindle checkpoint response by monitoring mitotic timing after performing double depletion of *ani-2* and *zyg-1* in *san-1* and *pch-2;san-1* mutant embryos. SAN-1 is the *C. elegans*

ortholog of the essential spindle checkpoint factor, Mad3 (Nystul et al., 2003) (Figure S1B). There was no significant difference between the slopes of the regression analysis of *san-1* and *pch-2;san-1* data (p value = 0.8813). These data allow us to draw two important conclusions: 1) Since we observe a robust spindle checkpoint activation in *pch-2* mutant embryos as they decrease in size and mitotic timing is similar to what we observe in control embryos, PCH-2 does not appear to affect spindle checkpoint silencing in *C. elegans*; and 2) PCH-2's requirement during spindle checkpoint activation is proportional to cell volume in somatic cells of two-cell *C. elegans* embryos.

PCH-2 becomes dispensable for MAD-2 recruitment at unattached kinetochores in somatic cells as they decrease in size

Recent experiments have shown that acute depletion of PCH-2's mammalian ortholog, TRIP13, has no effect on spindle checkpoint function in HeLa cells until O-Mad2 is limiting (Ma and Poon, 2018). Since MAD-2 is localized to the nucleus and nuclear envelope in *C. elegans* oocytes (Bohr et al., 2015; Lawrence et al., 2015) (Figure 2A) and *ani-2^{RNAi}* treatment does not affect nuclear size (Figure S2), we reasoned that as cells decrease in cell volume, the absolute amount of MAD-2 protein is likely to remain constant but its concentration increases. This increase in concentration may improve the likelihood that O-Mad2 is at or near unattached kinetochores, obviating the requirement for PCH-2 in small embryos.

To test this model, we quantified MAD-2 recruitment at unattached kinetochores in pseudo-metaphase in small control and *pch-2* mutant embryos (less than $3.5 \times 10^3 \mu\text{m}^3$) expressing GFP::MAD-2 and compared it to the recruitment observed in wild-type sized embryos. Consistent with our previous results, GFP::MAD-2 was recruited to 20% of control levels in *pch-2* mutant embryos that were wild-type in size (Nelson et al., 2015)

(Figure 2C). In small embryos, GFP::MAD-2 was recruited to unattached kinetochores in control embryos as expected (Figure 2B). In small *pch-2* mutant embryos, GFP::MAD-2 signal can be detected at unattached kinetochores (Figure 2B) and, when quantified, GFP::MAD-2 was partially restored to 58% of control levels (Figure 2C). One explanation for why GFP::MAD-2 recruitment is not completely restored in small *pch-2* mutant embryos may be that these smaller embryos require less MAD-2 recruitment to support a mitotic delay comparable to control small embryos (Défachelles et al., 2015). Nonetheless, our experiments demonstrate that PCH-2 is also dispensable for Mad2 recruitment at unattached kinetochores in small embryos, potentially because decreasing cell volume concentrates Mad2, specifically O-Mad2.

PCH-2 is required for the spindle checkpoint response during embryogenesis

During embryogenesis, cell volume decreases and spindle checkpoint strength increases (Galli and Morgan, 2016; Gerhold et al., 2018). Given our observation, that PCH-2 becomes dispensable as cell volume decreases in the AB cell of two-cell embryos, we tested whether this also happens during normal embryogenesis. We permeabilized embryos by performing *perm-1* RNAi (Carvalho et al., 2011) and activated the spindle checkpoint by treating these *perm-1*^{RNAi} embryos with nocodazole, a drug that depolymerizes microtubules. Since we could not always reliably visualize OCC in these dividing embryos, we measured mitotic timing from nuclear envelope break down (NEBD) to the nuclear envelope reformation (NER) for each stage of embryogenesis. Consistent with previous reports, cells in control embryos exhibited a longer mitotic delay in 16-cell than in 4-cell embryos, indicating that the spindle checkpoint increases in strength as cells decrease in volume during embryogenesis (Galli and Morgan, 2016; Gerhold et al., 2018). As a control, we performed the same experiment in *san-1* mutants and did not detect a mitotic delay when these embryos were treated with nocodazole

(Figure 3A). In stark contrast to our *ani-2^{RNAi}* experiments, the mitotic timing observed in *pch-2* mutant embryos treated with nocodazole was similar to *san-1* mutant embryos treated with nocodazole. Thus, as cells naturally decrease in cell size during embryogenesis, PCH-2 remains essential for the spindle checkpoint.

We also tested if a subtle increase in MAD-2 protein levels would suppress the spindle checkpoint defect in *pch-2* mutant embryos. The presence of a GFP::MAD-2 transgene, in addition to endogenous MAD-2, results in about 2.5 times more MAD-2 in embryos. This slight overexpression generates a normal spindle checkpoint response in control AB cells and can bypass the requirement for checkpoint components MAD-3 or BUB-3 (Essex et al., 2009), but not PCH-2 (Nelson et al., 2015). We found that overexpression of MAD-2 in control and *pch-2* mutant 4- and 16-cell embryos treated with nocodazole behaved similarly as their counterparts with normal levels of MAD-2 (Figure 3B). These results confirm that PCH-2 is essential for the spindle checkpoint during normal embryogenesis, suggesting that Mad2 may undergo additional regulation during embryogenesis that requires PCH-2 to make O-Mad2 available even as cells decrease in size. Further, additional considerations may make direct comparisons between our *ani-2^{RNAi};zyg-1^{RNAi}* experiments and dividing embryos treated with nocodazole difficult (see Discussion).

PCH-2 is responsible for the stronger spindle checkpoint in the germline lineage

Cell fate is another important determinant of spindle checkpoint strength. In *C. elegans* embryos, the spindle checkpoint is stronger in germline precursor cells than similarly sized somatic counterparts (Galli and Morgan, 2016; Gerhold et al., 2018).

Therefore, we tested whether PCH-2 contributed to the stronger spindle checkpoint in the germline lineage, specifically in P₁ cells of two-cell embryos (Figure 4). Consistent

with other reports (Galli and Morgan, 2016; Gerhold et al., 2018), when we performed double depletion of *ani-2* and *zyg-1* in control embryos and monitored mitotic timing, we observed P₁ cells with similar volumes as AB cells exhibiting a longer cell cycle delay (Figure 4A). Further, the regression analysis that best fit control P₁ data is significantly different and steeper than that of control AB cells (p value < 0.0001), suggesting that variables in addition to cell volume contribute to the spindle checkpoint strength in germline precursor cells. When we knocked down both *ani-2* and *zyg-1* in *pch-2* mutant embryos, we no longer observed a significant difference (p value = 0.9096) between the slopes of the regression analysis of P₁ and AB cells (Figure 4B), indicating that PCH-2 is responsible for the stronger checkpoint in P₁ cells.

We observed that cell cycle timing was faster in *pch-2* mutant P₁ cells than similarly sized *pch-2* mutant AB cells after treatment with *ani-2* and *zyg-1* RNAi (Figure 4B). We wondered if embryonic germline precursor cells might rely on spindle checkpoint proteins for normal mitotic timing, analogous to mitotically dividing stem cells in the *C. elegans* germline (Gerhold et al., 2015) and similar to mammalian cultured cells (Meraldi, 2004; Rodriguez-Bravo, 2014; Ma and Poon, 2016). To address this, we measured normal mitotic timing in AB and P₁ cells of both control and *pch-2* mutant embryos. We found that while normal mitotic timing is unaffected by mutation of *pch-2* in AB cells, *pch-2* mutant P₁ cells go through mitosis significantly faster than control P₁ cells (Figure 4C), thus providing an explanation for the faster cell cycle timing in *pch-2* mutant P₁ cells with the same cell volume as *pch-2* mutant AB cells after treatment with *ani-2* and *zyg-1* RNAi.

PCH-2's enrichment in P₁ cells is dependent on PAR-1

Cell fate is driven by the asymmetric distribution of various determinants between somatic and germline lineages during early divisions of the *C. elegans* embryo (reviewed in Rose and Gönczy, 2014). Since we found that PCH-2 promoted the spindle checkpoint strength in both AB and P₁ cells, but even more dramatically in P₁ cells, we asked if PCH-2 was regulated differently between these cells. We previously generated a tagged version of PCH-2 at the endogenous locus, PCH-2::GFP, that could be visualized at unattached kinetochores at the pseudo-metaphase plate and rescued checkpoint function in AB cells (Nelson et al., 2015). We tested whether this transgene could also support the stronger checkpoint in P₁ cells. We treated embryos expressing PCH-2::GFP with *zyg-1* RNAi and evaluated mitotic timing in both AB and P₁ cells, in the presence or absence of monopolar spindles, using chromosome decondensation as a marker for mitotic exit. P₁ cells expressing PCH-2::GFP had full checkpoint function, exhibiting a mitotic delay longer than AB cells also expressing PCH-2::GFP (Figure 5A).

Previous transcriptome analysis of PCH-2 did not reveal asymmetric enrichment of PCH-2 mRNA between AB and P₁ cells (Tintori et al., 2016). We tested whether PCH-2::GFP exhibited differences in protein levels between AB and P₁ cells. First, we assessed whether PCH-2::GFP was more enriched in pseudo-metaphase at unattached kinetochores in P₁ than AB cells. We quantified PCH-2::GFP fluorescence at unattached kinetochores in both AB and P₁ cells of embryos treated with *zyg-1* RNAi but did not detect any difference between the two cell types (Figures S3A and B). Similarly, we did not detect any difference in GFP::MAD-2 recruitment at unattached kinetochores between AB and P₁ cells in *zyg-1*^{RNAi} embryos (Figures S3C and D).

Next, we quantified PCH-2::GFP fluorescence in AB and P₁ cells during unperturbed cell cycles. In the AB cell, PCH-2 protein becomes enriched in the area around the

chromosomes in prometaphase (Nelson et al., 2015). We observed similar localization of PCH-2::GFP in P₁ cells (Figure 5B). When we quantified the fluorescence of PCH-2::GFP in this area surrounding chromosomes after NEBD in both AB and P₁ cells, we detected a statistically significant enrichment of PCH-2::GFP in P₁ cells (Figure 5C). This enrichment is not the indirect consequence of the smaller volume of P₁ cells since we did not observe a difference in the fluorescence of PCH-2::GFP in the cytoplasm between AB and P₁ cells (Figure S4), demonstrating that PCH-2::GFP is more highly enriched in P₁ cells than AB cells.

To better understand the relationship between PCH-2 enrichment in P₁ cells and cell fate, we abrogated the asymmetry of the two-cell embryo by performing RNAi against the essential polarity factor, PAR-1 (Guo and Kemphues, 1995). In *par-1*^{RNAi} mutant embryos, AB and P₁ cells exhibit the same checkpoint strength (Gerhold et al., 2018), indicating that the stronger spindle checkpoint response in the P₁ cells depends on this asymmetric division. We quantified PCH-2::GFP fluorescence in the area around chromosomes in AB and P₁ cells after *par-1* RNAi and observed that the fluorescence of PCH-2::GFP was not significantly different between AB and P₁ cells, unlike what we observed in embryos exposed to control RNAi (Figure 5D). Therefore, PCH-2::GFP's enrichment in P₁ cells depends on a conserved factor that induces embryonic asymmetry and germline cell fate.

The stronger checkpoint in P₁ cells depends on CMT-1

In vitro, the *C. elegans* ortholog of p31^{comet}, CMT-1, is required for PCH-2 to bind and remodel Mad2 from the closed conformation to the open one (Ye et al., 2015). In addition to this role, CMT-1 is also required to localize PCH-2 to unattached kinetochores during the spindle checkpoint response, stabilize Mad2 protein levels and

generate a robust spindle checkpoint response in AB cells (Nelson et al., 2015). Overexpressing Mad2 does not suppress the partial defect in spindle checkpoint activation in *cmt-1* mutants (Nelson et al., 2015), suggesting that PCH-2's localization to unattached kinetochores promotes a strong spindle checkpoint response in large AB cells. Therefore, we reasoned that CMT-1 might also be required for the stronger checkpoint in P₁ cells.

To test this possibility, we performed *zyg-1* RNAi on control and *cmt-1* mutant embryos and monitored mitotic timing in both AB and P₁ cells. AB and P₁ cells of control and *cmt-1* mutant embryos treated with control RNAi had similar mitotic timing. In *zyg-1*^{RNAi} embryos, P₁ cells exhibited a stronger checkpoint response than AB cells. By contrast, both AB and P₁ cells in *cmt-1*;*zyg-1*^{RNAi} mutant embryos exhibited similar spindle checkpoint delays (Figure 6A). Despite having spindle checkpoint responses that were less robust than that of control *zyg-1*^{RNAi} embryos, AB and P₁ cells in *cmt-1* mutant embryos treated with *zyg-1* RNAi spent significantly longer in mitosis than *cmt-1* mutant embryos treated with control RNAi, indicating that they activated a weaker spindle checkpoint response, similar to our published results (Nelson et al., 2015). More importantly, *cmt-1*;*zyg-1*^{RNAi} mutant embryos failed to generate a stronger checkpoint in P₁ cells, indicating that CMT-1 is also essential to promote checkpoint strength in germline precursor cells.

Aside from localizing PCH-2 to unattached kinetochores, we wondered if CMT-1 was required for any other aspects of PCH-2 regulation. Therefore, we tested whether CMT-1 was necessary for PCH-2's asymmetric enrichment in P₁ cells. We quantified PCH-2::GFP fluorescence in prometaphase in the area around chromosomes in both *cmt-1* mutant AB and P₁ cells (Figure 6B). First, we found that PCH-2::GFP fluorescence was

similar between AB cells in both control and *cmt-1* mutant embryos (Figure 6C), consistent with our hypothesis that the weaker checkpoint in *cmt-1* AB cells is a consequence of the absence of PCH-2 recruitment at unattached kinetochore (Nelson et al., 2015). Further, when we compared the quantification of PCH-2::GFP fluorescence in *cmt-1* mutant AB and P₁ cells, we did not detect a significant difference between the two cells (Figure 6D), unlike our experiment in control embryos (Figure 5C). Thus, while we favor the hypothesis that CMT-1's role in promoting spindle checkpoint strength in both AB and P₁ cells is the product of localizing PCH-2 to unattached kinetochores, based on the reduced robustness of the spindle checkpoint in *cmt-1* mutants (Figure 6) and our *ani-2^{RNAi};zyg-1^{RNAi}* experiments (Figures 1 and 2), it's likely that CMT-1's contribution to the asymmetric enrichment of PCH-2 in P₁ cells also contributes to the stronger spindle checkpoint in these cells.

DISCUSSION

The role of PCH-2, and its mammalian ortholog TRIP13, in the spindle checkpoint has been enigmatic. Originally identified as a checkpoint silencing factor (Wang et al., 2014; Eytan et al., 2014; Ye et al., 2015; Miniowitz-Shemtov et al., 2015; Brulotte et al., 2017; Alfieri et al., 2018), more recent evidence also indicates a role in promoting the checkpoint response (Nelson et al., 2015; Ma and Poon, 2016; Yost et al., 2017). It's clear that the reliance on PCH-2/TRIP13 in checkpoint activation likely reflects the relative levels and availability of O-Mad2 (Ma and Poon, 2018). We show here that PCH-2's role in regulating O-Mad2 availability, specifically at or near unattached kinetochores, also controls checkpoint strength, providing an unanticipated mechanism to explain its regulation (Figure 7). We propose that this role in checkpoint strength is particularly

important in large cells, such as oocytes and cells in early embryos, as well as cells that give rise to immortal germ cells.

A prediction of our model is that overexpression of Mad2 should also make PCH-2 dispensable for the spindle checkpoint activation. We've shown that subtle elevations of Mad2 protein levels cannot suppress the requirement for PCH-2 in two-cell embryos (Nelson et al., 2015). Unfortunately, more dramatic overexpression experiments are technically difficult in *C. elegans*. Further, it's likely that strong overexpression of Mad2 in *C. elegans* embryos will delay normal mitosis, consistent with similar findings in mammalian cells (Marks et al., 2017) and budding yeast (Mariani et al., 2012). In this way, PCH-2's function may provide a useful buffer: Since Mad2 protein levels may need to stay within a narrow range to allow normal mitotic timing, PCH-2's localization at or near unattached kinetochores provide a mechanism to increase O-Mad2's local concentration to promote effective and efficient signaling during checkpoint activation.

Despite our findings that PCH-2 becomes dispensable for spindle checkpoint activation as two-cell embryos decrease in volume, PCH-2 remains essential for the spindle checkpoint as cells normally decrease in volume during embryogenesis (Figure 3), indicating that relative levels of O-Mad2 and C-Mad2 may be further regulated during embryonic development. This possibility is supported by our finding that PCH-2 regulates normal cell cycle timing in P₁ cells, but not AB cells (Figure 4C), which suggests that variations in O-Mad2/C-Mad2 ratios influence normal mitotic timing in cells with specific developmental fates. In addition, unlike the nuclei of two-cell embryos treated with *ani-2*^{RNAi} (Figure S2), nuclear volume scales with cell volume during embryogenesis (Gerhold et al., 2018). Therefore, the concentration of Mad2 may not necessarily increase as cell size decreases in cells of the developing embryo, making

direct comparisons between small cells obtained by *ani-2^{RNAi}* treatment and small cells resulting from normal embryogenesis challenging.

Our experiments identify CMT-1, the *C. elegans* ortholog of mammalian p31^{comet}, as an important regulator of PCH-2 function and, as a result, checkpoint strength. In addition to its requirement in facilitating PCH-2's ability to interact with its substrate, Mad2 (Ye et al., 2015; Miniowitz-Shemtov et al., 2015; Brulotte et al., 2017; Alfieri et al., 2018), CMT-1 localizes PCH-2 to unattached kinetochores (Nelson et al., 2015) and promotes PCH-2's enrichment in P₁ cells (Figure 6). We propose that both of these roles contribute to checkpoint strength. In large AB cells, CMT-1 ensures PCH-2's presence at unattached kinetochores, increasing the local concentration of O-Mad2 and driving the production of soluble C-Mad2 and MCC (Figure 7A). In P₁ cells, the combination of PCH-2's localization at kinetochores and its enrichment promotes a checkpoint stronger than somatic cells (Figure 7C). It's striking that P₁ cells, which are slightly smaller than AB cells, exhibit similar checkpoint strength to AB cells when CMT-1 is absent (Figure 6). This indicates that even these cells depend on PCH-2 to be present at unattached kinetochores to increase the local concentration of O-Mad2 and promote checkpoint strength.

Evolutionary analysis across phyla have revealed a close co-evolutionary relationship between PCH-2 and its orthologs and HORMA domain containing proteins, including CMT-1 and Mad2 (Vleugel et al., 2012; van Hooff et al., 2017). However, some organisms that rely on the templated conversion of O-Mad2 to C-Mad2 to assemble the MCC, such as budding and fission yeasts (Nezi et al., 2006; Chao et al., 2012) either don't express their PCH-2 ortholog during mitosis (budding yeast) (San-Segundo and Roeder, 1999) or don't have a PCH-2 ortholog in their genome (fission yeast) (Wu and

Burgess, 2006). This is potentially explained by cell volume: Both budding and fission yeasts are two orders of magnitude smaller than mammalian cells and *C. elegans* embryos. They also undergo closed mitosis, in which the nuclear envelope does not break down, providing an additional opportunity to concentrate factors required for mitosis. We propose that recruiting O-Mad2 to unattached kinetochores may not present as great a challenge in these significantly smaller cells, making a factor required to increase the local concentration of O-Mad2 at unattached kinetochores unnecessary.

An obvious question our experiments raise is how PCH-2 is enriched in P₁ cells. Germline precursor cells are transcriptionally silent until gastrulation (Seydoux et al., 1996) and sequencing of mRNA in early embryos shows that both CMT-1 and PCH-2 mRNA are not enriched in germline precursor cells (Tintori et al., 2016), indicating that enrichment of PCH-2 is likely to occur at the level of protein regulation. Understanding this regulation, its control by developmental events and its effect on the relative levels of O-Mad2 and C-Mad2 in different cell types promises to be an exciting area of investigation.

ACKNOWLEDGEMENTS

We would like to thank Arshad Desai, Karen Oegema, Susan Strome and David Morgan for valuable strains and reagents. This work was supported by the NIH (grant numbers T32GM008646 [C.R.N. and A.R.] and R01GM097144 [N.B.]). Some strains were provided by the CGC, which is funded by NIH Office of Research Infrastructure Programs (P40 OD010440).

REFERENCES

- Alfieri, C., Chang, L., and Barford, D. (2018). Mechanism for remodelling of the cell cycle checkpoint protein MAD2 by the ATPase TRIP13. *Nature*.
- Aravind, L., and Koonin, E.V. (1998). The HORMA domain: a common structural denominator in mitotic checkpoints, chromosome synapsis and DNA repair. *Trends Biochem. Sci.* 23, 284–286.
- Bhalla, N., and Dernburg, A.F. (2005). A Conserved Checkpoint Monitors Meiotic Chromosome Synapsis in *Caenorhabditis elegans*. *Science* 310, 1683–1686.
- Bohr, T., Nelson, C.R., Klee, E., and Bhalla, N. (2015). Spindle assembly checkpoint proteins regulate and monitor meiotic synapsis in *C. elegans*. *J. Cell Biol.* 211, 233–242.
- Brenner, S. (1974). The genetics of *Caenorhabditis elegans*. *Genetics* 77, 71–94.
- Brulotte, M.L., Jeong, B.-C., Li, F., Li, B., Yu, E.B., Wu, Q., Brautigam, C.A., Yu, H., and Luo, X. (2017). Mechanistic insight into TRIP13-catalyzed Mad2 structural transition and spindle checkpoint silencing. *Nat. Commun.* 8, 1956.
- Carvalho, A., Olson, S.K., Gutierrez, E., Zhang, K., Noble, L.B., Zanin, E., Desai, A., Groisman, A., and Oegema, K. (2011). Acute drug treatment in the early *C. elegans* embryo. *PloS One* 6, e24656.
- Chao, W.C.H., Kulkarni, K., Zhang, Z., Kong, E.H., and Barford, D. (2012). Structure of the mitotic checkpoint complex. *Nature* 484, 208–213.
- Chen, C., Jomaa, A., Ortega, J., and Alani, E.E. (2014). Pch2 is a hexameric ring ATPase that remodels the chromosome axis protein Hop1. *Proc. Natl. Acad. Sci. U. S. A.* 111, E44–E53.

556 Chen, R.H., Waters, J.C., Salmon, E.D., and Murray, A.W. (1996). Association of spindle
557 assembly checkpoint component XMad2 with unattached kinetochores. *Science* 274,
558 242–246.

559 Chen, R.H., Shevchenko, A., Mann, M., and Murray, A.W. (1998). Spindle checkpoint
560 protein Xmad1 recruits Xmad2 to unattached kinetochores. *J. Cell Biol.* 143, 283–295.

561 Collin, P., Nashchekina, O., Walker, R., and Pines, J. (2013). The spindle assembly
562 checkpoint works like a rheostat rather than a toggle switch. *Nat. Cell Biol.* 15, 1378–
563 1385.

564 Davis, L.I., and Blobel, G. (1986). Identification and characterization of a nuclear pore
565 complex protein. *Cell* 45, 699–709.

566 De Antoni, A., Pearson, C.G., Cimini, D., Canman, J.C., Sala, V., Nezi, L., Mapelli, M.,
567 Sironi, L., Faretta, M., Salmon, E.D., et al. (2005). The Mad1/Mad2 complex as a
568 template for Mad2 activation in the spindle assembly checkpoint. *Curr. Biol. CB* 15, 214–
569 225.

570 Défachelles, L., Hainline, S.G., Menant, A., Lee, L.A., and Karess, R.E. (2015). A
571 maternal effect rough deal mutation suggests that multiple pathways regulate *Drosophila*
572 RZZ kinetochore recruitment. *J Cell Sci* 128, 1204–1216.

573 Dick, A.E., and Gerlich, D.W. (2013). Kinetic framework of spindle assembly checkpoint
574 signalling. *Nat. Cell Biol.* 15, 1370–1377.

575 Edelstein, A.D., Tsuchida, M.A., Amodaj, N., Pinkard, H., Vale, R.D., and Stuurman, N.
576 (2014). Advanced methods of microscope control using µManager software. *J. Biol.*
577 *Methods* 1.

Essex, A., Dammermann, A., Lewellyn, L., Oegema, K., and Desai, A. (2009).
Systematic analysis in *Caenorhabditis elegans* reveals that the spindle checkpoint is
composed of two largely independent branches. *Mol. Biol. Cell* 20, 1252–1267.

Eytan, E., Wang, K., Miniowitz-Shemtov, S., Sitry-Shevah, D., Kaisari, S., Yen, T.J., Liu,
S.-T., and Hershko, A. (2014). Disassembly of mitotic checkpoint complexes by the joint
action of the AAA-ATPase TRIP13 and p31comet. *Proc. Natl. Acad. Sci. U. S. A.* 111,
12019–12024.

Fava, L.L., Kaulich, M., Nigg, E.A., and Santamaria, A. (2011). Probing the in vivo
function of Mad1:C-Mad2 in the spindle assembly checkpoint. *EMBO J.* 30, 3322–3336.

Galli, M., and Morgan, D.O. (2016). Cell Size Determines the Strength of the Spindle
Assembly Checkpoint during Embryonic Development. *Dev. Cell* 36, 344–352.

Gerhold, A.R., Ryan, J., Vallée-Trudeau, J.-N., Dorn, J.F., Labbé, J.-C., and Maddox,
P.S. (2015). Investigating the regulation of stem and progenitor cell mitotic progression
by in situ imaging. *Curr. Biol. CB* 25, 1123–1134.

Gerhold, A.R., Poupart, V., Labbé, J.-C., and Maddox, P.S. (2018). Spindle assembly
checkpoint strength is linked to cell fate in the *C. elegans* embryo. *Mol. Biol. Cell*
mbcE18040215.

Guo, S., and Kemphues, K.J. (1995). *par-1*, a gene required for establishing polarity in
C. elegans embryos, encodes a putative Ser/Thr kinase that is asymmetrically
distributed. *Cell* 81, 611–620.

598 van Hooff, J.J., Tromer, E., van Wijk, L.M., Snel, B., and Kops, G.J. (2017). Evolutionary
599 dynamics of the kinetochore network in eukaryotes as revealed by comparative
600 genomics. *EMBO Rep.* 18, 1559–1571.

601 Kyogoku, H., and Kitajima, T.S. (2017). Large Cytoplasm Is Linked to the Error-Prone
602 Nature of Oocytes. *Dev. Cell* 41, 287-298.e4.

603 Lawrence, K.S., Chau, T., and Engebrecht, J. (2015). DNA damage response and
604 spindle assembly checkpoint function throughout the cell cycle to ensure genomic
605 integrity. *PLoS Genet.* 11, e1005150.

606 Li, Y., and Benezra, R. (1996). Identification of a human mitotic checkpoint gene:
607 hsMAD2. *Science* 274, 246–248.

608 Luo, X., Tang, Z., Rizo, J., and Yu, H. (2002). The Mad2 spindle checkpoint protein
609 undergoes similar major conformational changes upon binding to either Mad1 or Cdc20.
610 *Mol. Cell* 9, 59–71.

611 Luo, X., Tang, Z., Xia, G., Wassmann, K., Matsumoto, T., Rizo, J., and Yu, H. (2004).
612 The Mad2 spindle checkpoint protein has two distinct natively folded states. *Nat. Struct.*
613 *Mol. Biol.* 11, 338–345.

614 Ma, H.T., and Poon, R.Y.C. (2016). TRIP13 Regulates Both the Activation and
615 Inactivation of the Spindle-Assembly Checkpoint. *Cell Rep.* 14, 1086–1099.

616 Ma, H.T., and Poon, R.Y.C. (2018). TRIP13 Functions in the Establishment of the
617 Spindle Assembly Checkpoint by Replenishing O-MAD2. *Cell Rep.* 22, 1439–1450.

618 Maddox, A.S., Habermann, B., Desai, A., and Oegema, K. (2005). Distinct roles for two
619 *C. elegans* anillins in the gonad and early embryo. *Dev. Camb. Engl.* 132, 2837–2848.

620 Mariani, L., Chiroli, E., Nezi, L., Muller, H., Piatti, S., Musacchio, A., and Ciliberto, A.
621 (2012). Role of the Mad2 dimerization interface in the spindle assembly checkpoint
622 independent of kinetochores. *Curr. Biol.* **22**, 1900–1908.

623 Marks, D.H., Thomas, R., Chin, Y., Shah, R., Khoo, C., and Benezra, R. (2017). Mad2
624 Overexpression Uncovers a Critical Role for TRIP13 in Mitotic Exit. *Cell Rep.* **19**, 1832–
625 1845.

626 Miniowitz-Shemtov, S., Eytan, E., Kaisari, S., Sitry-Shevah, D., and Hershko, A. (2015).
627 Mode of interaction of TRIP13 AAA-ATPase with the Mad2-binding protein p31comet
628 and with mitotic checkpoint complexes. *Proc. Natl. Acad. Sci. U. S. A.* **112**, 11536–
629 11540.

630 Moyle, M.W., Kim, T., Hattersley, N., Espeut, J., Cheerambathur, D.K., Oegema, K., and
631 Desai, A. (2014). A Bub1–Mad1 interaction targets the Mad1–Mad2 complex to
632 unattached kinetochores to initiate the spindle checkpoint. *J. Cell Biol.* **204**, 647–657.

633 Nelson, C.R., Hwang, T., Chen, P.-H., and Bhalla, N. (2015). TRIP13PCH-2 promotes
634 Mad2 localization to unattached kinetochores in the spindle checkpoint response. *J. Cell*
635 *Biol.* **211**, 503–516.

636 Nezi, L., Rancati, G., De Antoni, A., Pasqualato, S., Piatti, S., and Musacchio, A. (2006).
637 Accumulation of Mad2-Cdc20 complex during spindle checkpoint activation requires
638 binding of open and closed conformers of Mad2 in *Saccharomyces cerevisiae*. *J. Cell*
639 *Biol.* **174**, 39–51.

640 Nystul, T.G., Goldmark, J.P., Padilla, P.A., and Roth, M.B. (2003). Suspended animation
641 in *C. elegans* requires the spindle checkpoint. *Science* **302**, 1038–1041.

642 O'Connell, K.F., Caron, C., Kopish, K.R., Hurd, D.D., Kempfues, K.J., Li, Y., and White,
643 J.G. (2001). The *C. elegans* *zyg-1* gene encodes a regulator of centrosome duplication
644 with distinct maternal and paternal roles in the embryo. *Cell* 105, 547–558.

645 Rose, L., and Gönczy, P. (2014). Polarity establishment, asymmetric division and
646 segregation of fate determinants in early *C. elegans* embryos. *WormBook Online Rev. C*
647 *Elegans Biol.* 1–43.

648 San-Segundo, P.A., and Roeder, G.S. (1999). Pch2 links chromatin silencing to meiotic
649 checkpoint control. *Cell* 97, 313–324.

650 Seydoux, G., Mello, C.C., Pettitt, J., Wood, W.B., Priess, J.R., and Fire, A. (1996).
651 Repression of gene expression in the embryonic germ lineage of *C. elegans*. *Nature*
652 382, 713–716.

653 Sironi, L., Melixetian, M., Faretta, M., Prosperini, E., Helin, K., and Musacchio, A. (2001).
654 Mad2 binding to Mad1 and Cdc20, rather than oligomerization, is required for the spindle
655 checkpoint. *EMBO J.* 20, 6371–6382.

656 Sironi, L., Mapelli, M., Knapp, S., De Antoni, A., Jeang, K.-T., and Musacchio, A. (2002).
657 Crystal structure of the tetrameric Mad1-Mad2 core complex: implications of a “safety
658 belt” binding mechanism for the spindle checkpoint. *EMBO J.* 21, 2496–2506.

659 Sudakin, V., Chan, G.K., and Yen, T.J. (2001). Checkpoint inhibition of the APC/C in
660 HeLa cells is mediated by a complex of BUBR1, BUB3, CDC20, and MAD2. *J. Cell Biol.*
661 154, 925–936.

662 Tintori, S.C., Osborne Nishimura, E., Golden, P., Lieb, J.D., and Goldstein, B. (2016). A
663 Transcriptional Lineage of the Early *C. elegans* Embryo. *Dev. Cell* 38, 430–444.

664 Tipton, A.R., Wang, K., Oladimeji, P., Sufi, S., Gu, Z., and Liu, S.-T. (2012). Identification
665 of novel mitosis regulators through data mining with human centromere/kinetochore
666 proteins as group queries. *BMC Cell Biol.* 13, 15.

667 Vader, G. (2015). Pch2(TRIP13): controlling cell division through regulation of HORMA
668 domains. *Chromosoma* 124, 333–339.

669 Vleugel, M., Hoogendoorn, E., Snel, B., and Kops, G.J.P.L. (2012). Evolution and
670 function of the mitotic checkpoint. *Dev. Cell* 23, 239–250.

671 Wang, K., Sturt-Gillespie, B., Hittle, J.C., Macdonald, D., Chan, G.K., Yen, T.J., and Liu,
672 S.-T. (2014). Thyroid Hormone Receptor Interacting Protein 13 (TRIP13) AAA-ATPase
673 Is a Novel Mitotic Checkpoint-silencing Protein. *J. Biol. Chem.* 289, 23928–23937.

674 Wu, H.-Y., and Burgess, S.M. (2006). Two distinct surveillance mechanisms monitor
675 meiotic chromosome metabolism in budding yeast. *Curr. Biol. CB* 16, 2473–2479.

676 Yang, M., Li, B., Tomchick, D.R., Machius, M., Rizo, J., Yu, H., and Luo, X. (2007).
677 p31comet blocks Mad2 activation through structural mimicry. *Cell* 131, 744–755.

678 Ye, Q., Rosenberg, S.C., Moeller, A., Speir, J.A., Su, T.Y., and Corbett, K.D. (2015).
679 TRIP13 is a protein-remodeling AAA+ ATPase that catalyzes MAD2 conformation
680 switching. *ELife* 4.

681 Yost, S., de Wolf, B., Hanks, S., Zachariou, A., Marcozzi, C., Clarke, M., de Voer, R.,
682 Etemad, B., Uijttewaai, E., Ramsay, E., et al. (2017). Biallelic TRIP13 mutations
683 predispose to Wilms tumor and chromosome missegregation. *Nat. Genet.* 49, 1148–
684 1151.

685

Figure Legends

Figure 1: PCH-2 becomes dispensable for the spindle checkpoint response in somatic cells as they decrease in size

(A) Images of control and *ani-2^{RNAi}* two-cell embryos. Scale bar indicates 5 μm . (B) Cartoon of embryos treated with *zyg-1^{RNAi}* or *ani-2^{RNAi}; zyg-1^{RNAi}*. (C) Mitotic timing in AB cells of control, *pch-2* and *mad-1* mutant embryos plotted against cell volume. Lines represent regression analysis for each set of data. (D) Data from (C) sorted into three categories: wild-type sized embryos (more than $5 \times 10^3 \mu\text{m}^3$), medium sized embryos (between $3.5 \times 10^3 \mu\text{m}^3$ and $5 \times 10^3 \mu\text{m}^3$) and small embryos (less than $3.5 \times 10^3 \mu\text{m}^3$). Error bars are S.E.M. In all graphs, a * indicates a p value < 0.05, ** indicates a p value < 0.01 and *** a p value < 0.0001.

Figure 2: PCH-2 becomes dispensable for MAD-2 recruitment at unattached kinetochores in somatic cells as they decrease in size

(A) Immunostaining of MAD-2 and nuclear pore complex components (NPCs) shows MAD-2 localized in the nucleus and at the nuclear envelope during interphase. Scale bar indicates 5 μm . (B) Cartoon and images of GFP::MAD-2 recruitment to unattached kinetochores in AB cells of small embryos. Scale bar 1 μm . (C) Quantification of kinetochore bound GFP::MAD-2. Error bars are S.E.M.

Figure 3: PCH-2 is required for the spindle checkpoint response during embryogenesis

(A) Mitotic timing in control, *pch-2* and *san-1* mutant embryos treated with nocodazole at different developmental stages (4- and 16-cell embryos). (B) Mitotic timing in control and

pch-2 mutant embryos overexpressing GFP::MAD-2 and treated with nocodazole at different developmental stages (4- and 16-cell embryos). Error bars are S.E.M.

Figure 4: PCH-2 is responsible for the stronger spindle checkpoint in the germline lineage

Mitotic timing in AB and P₁ cells plotted against cell volume in control *ani-2^{RNAi};zyg-1^{RNAi}* embryos (A) or *pch-2;ani-2^{RNAi};zyg-1^{RNAi}* (B) embryos. Lines represent regression analysis for each set of data. (C) Unperturbed mitotic timing of AB and P₁ cells in control and *pch-2* mutants. Error bars are S.E.M.

Figure 5: PCH-2's enrichment in P₁ cells depends on PAR-1

(A) Mitotic timing of control embryos and embryos expressing PCH-2::GFP during unperturbed divisions or in the presence of monopolar spindles. (B) Cartoon and images of PCH-2::GFP localization around mitotic chromosomes in AB and P₁ cells of two-cell embryos. Scale bar indicates 5 μm. (C) Quantification of PCH-2::GFP fluorescence in AB and P₁ cells. (D) Quantification of PCH-2::GFP fluorescence in AB and P₁ cells of *par-1^{RNAi}* embryos. Error bars are S.E.M. NS indicates not significant.

Figure 6: The stronger checkpoint in P₁ cells depends on CMT-1

(A) Mitotic timing of control, *cmt-1* and *mad-1* mutant embryos during unperturbed divisions or in the presence of monopolar spindles. (B) Cartoon and images of PCH-2::GFP localization around mitotic chromosomes in AB and P₁ cells of *cmt-1* mutant embryos. Scale bar indicates 5 μm. (C) Quantification of PCH-2::GFP fluorescence in AB cells of control and *cmt-1* mutant embryos. (D) Quantification of PCH-2::GFP fluorescence in AB and P₁ cells of *cmt-1* mutant embryos.

Figure 7: Model

(A) A robust spindle checkpoint response in large cells requires the presence of PCH-2 at unattached kinetochores to increase the local concentration O-MAD-2 at or near unattached kinetochores. (B) Reducing cell volume of two-cell embryos increases the concentration of O-Mad-2 near or at unattached kinetochores, allowing a checkpoint response in the absence of PCH-2. (C) The enrichment of PCH-2 in P₁ cells results in a higher production of O-MAD-2, generating a stronger spindle checkpoint response in P₁ cells.

Figure S1: Related to Figure 1. The mitotic delay observed in *pch-2;ani-2^{RNAi};zyg-1^{RNAi}* small cells is a spindle checkpoint response.

Cartoon of control and *ani-2^{RNAi}* two-cell embryos (A) and an *ani-2^{RNAi};zyg-1^{RNAi}* two-cell embryo (B). Mitotic timing in AB cells plotted against cell volume, during unperturbed mitosis (C) and in the presence of monopolar spindles (D). Lines represent regression analysis for each set of data.

Figure S2: Related to Figure 2. Nuclear volume does not scale with cell volume in *ani-2^{RNAi}* two-cell embryos.

(A) Images of a large (top) and small (bottom) AB cell of *ani-2^{RNAi}* embryos. The nuclear area is indicated with a dashed yellow line. Scale bar indicates 5 μ m (B) Nuclear area plotted against cell volume.

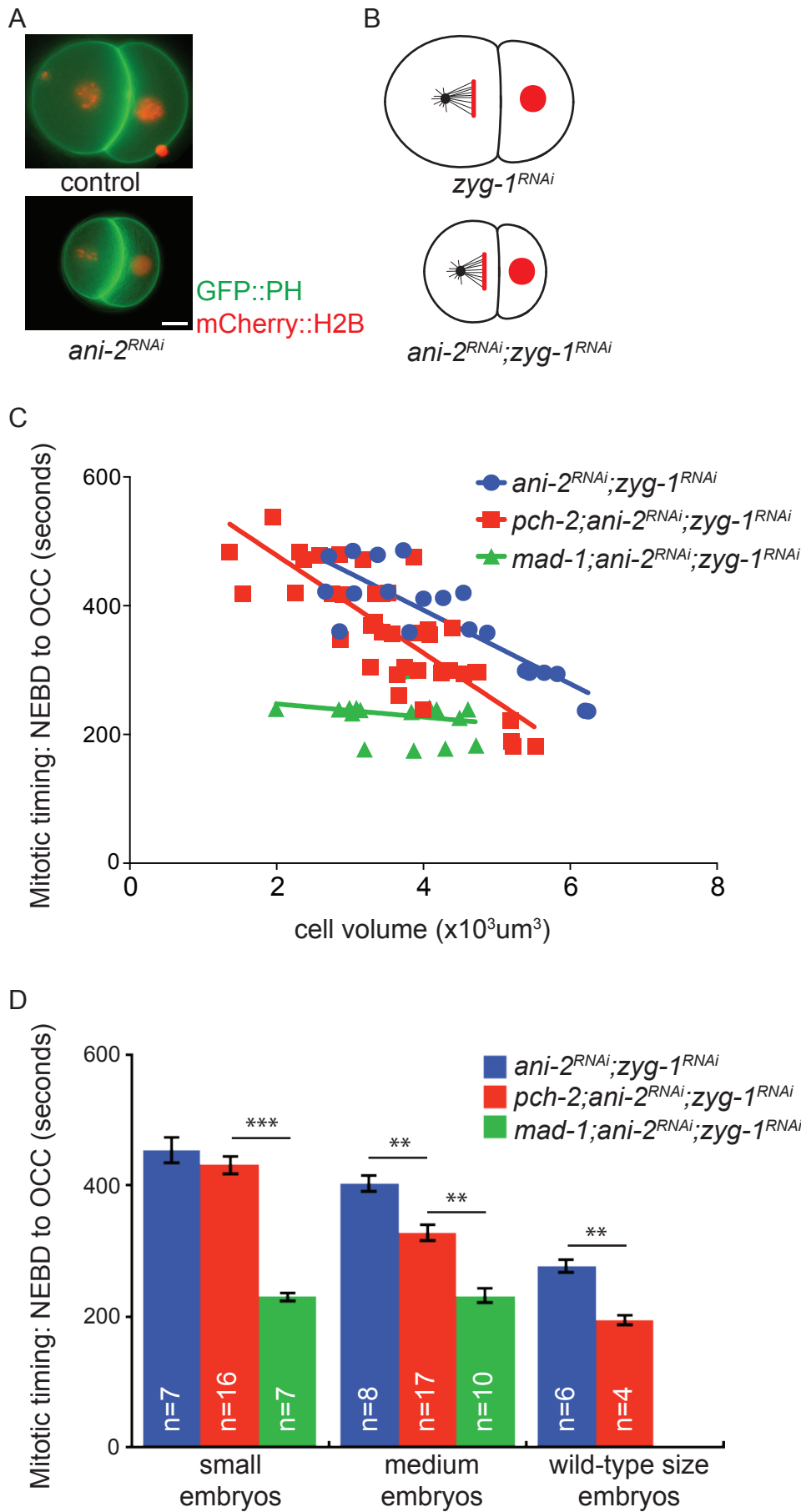
Figure S3: Related to Figure 5. There is no difference in the amount of PCH-2::GFP or GFP::MAD-2 recruited to unattached kinetochores in AB and P₁ cells.

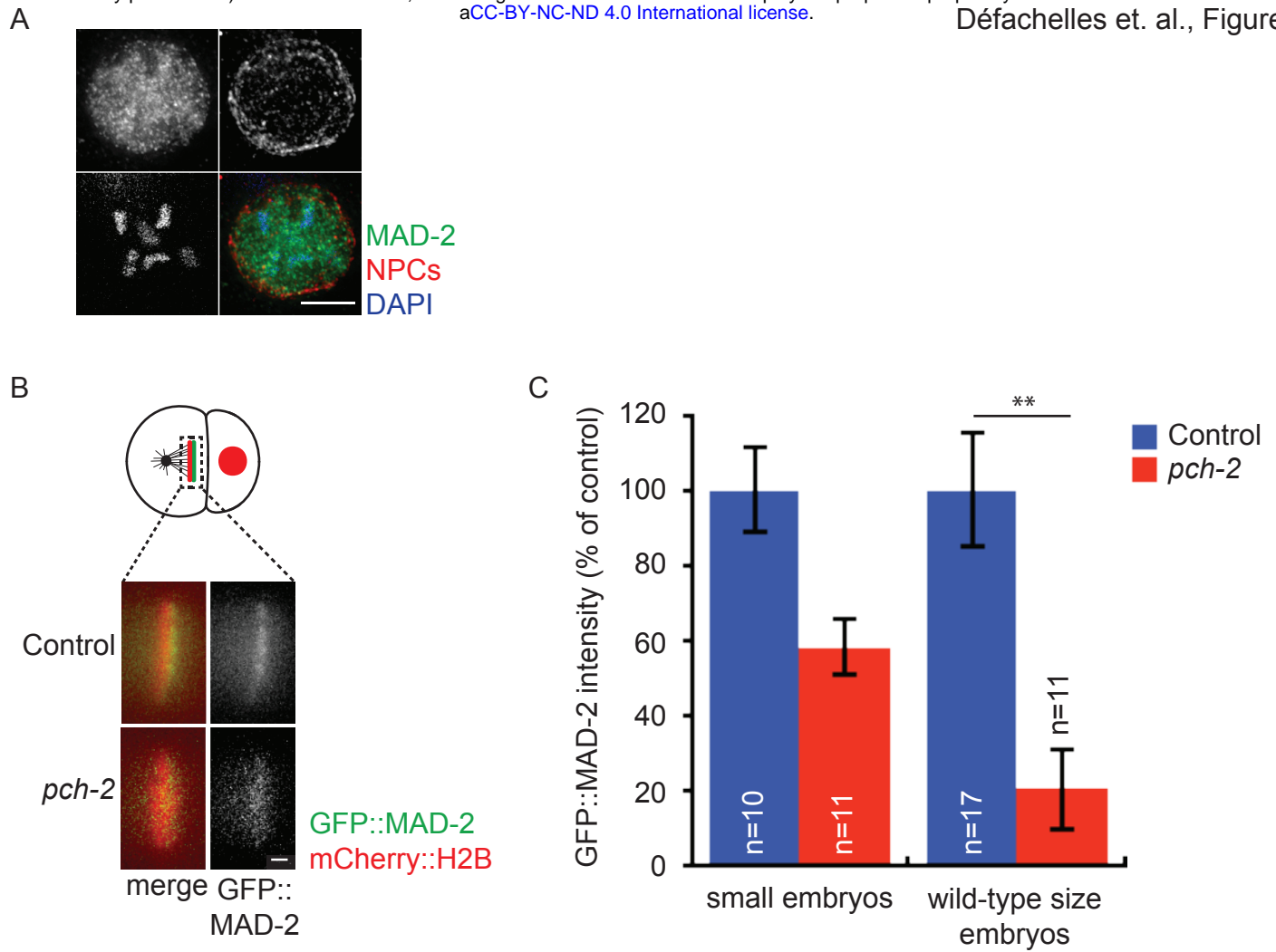
(A) Cartoon and images of PCH-2::GFP recruitment to unattached kinetochores in AB and P₁ cells of two-cell embryos. Scale bar indicates 1 μ m. (B) Quantification of PCH-

2::GFP recruitment at unattached kinetochores in AB and P₁ cells. (C) Cartoon and images of GFP::MAD-2 recruitment to unattached kinetochores in AB and P₁ cells of two-cell embryos. Scale bar indicates 1 μm. (D) Quantification of GFP::MAD-2 fluorescence at unattached kinetochores in AB and P₁ cells. Error bars are S.E.M. NS indicates not significant.

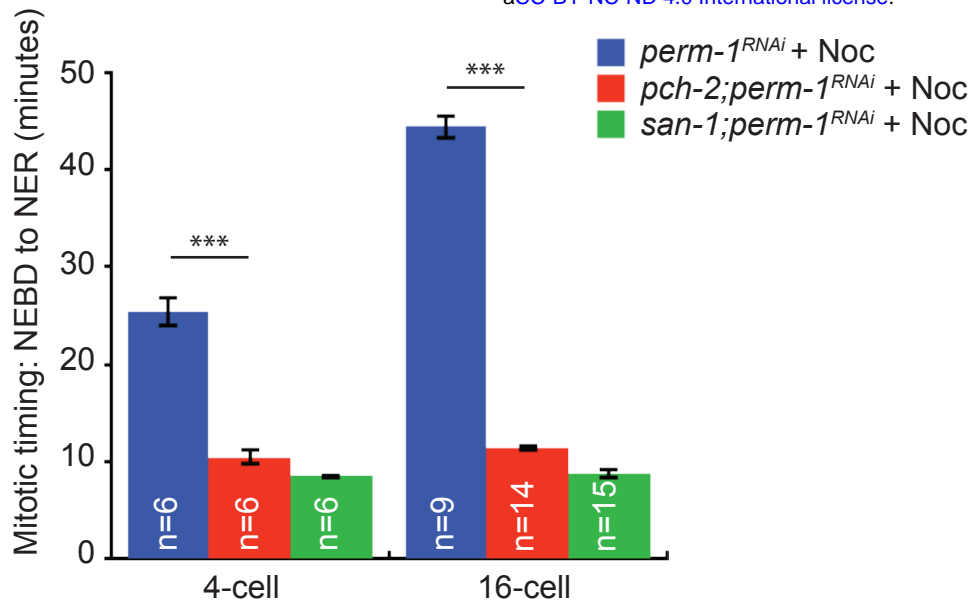
Figure S4: Related to Figure 5. There is no difference in the amount of PCH-2::GFP in the cytoplasm of AB and P₁ cells.

(A) Images of AB (left) and P₁ (right) cells after NEBD. Scale bar 5 μm. (B) Quantification of PCH-2::GFP fluorescence in the cytoplasm of AB and P₁ cells. Error bars are S.E.M.

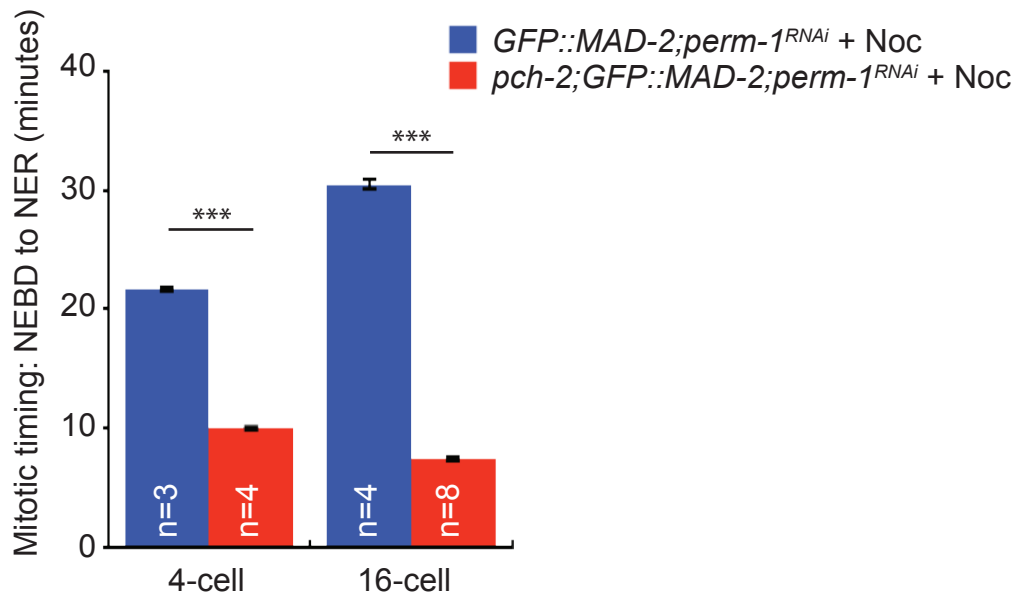




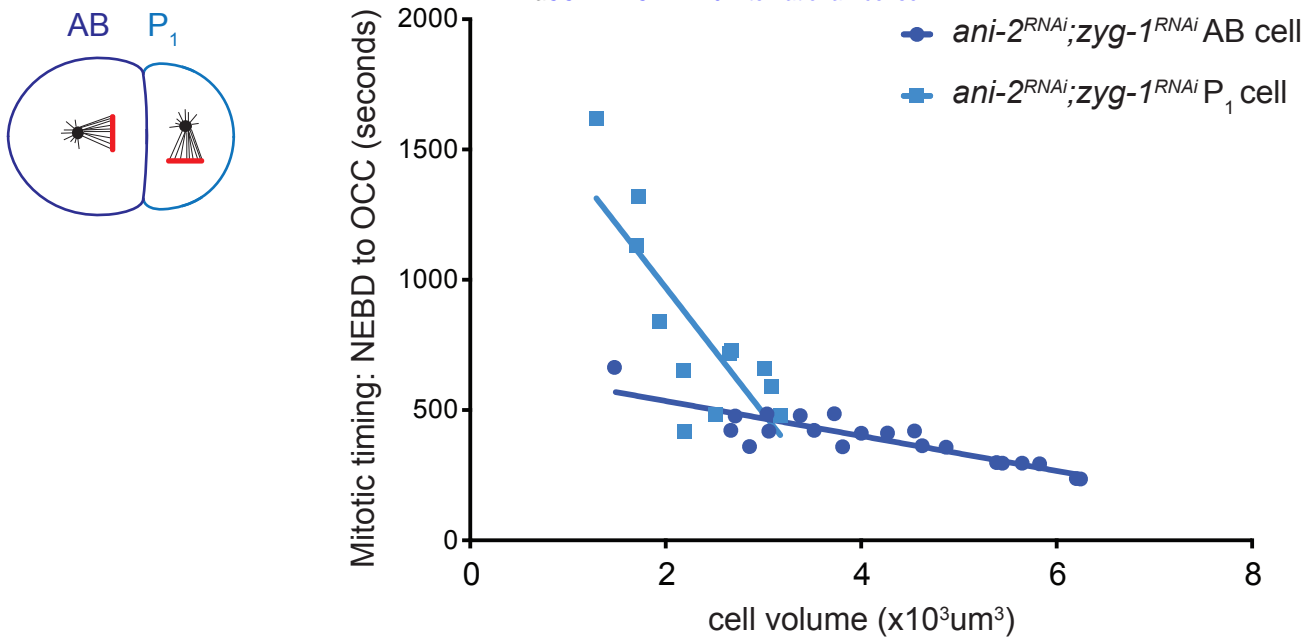
A



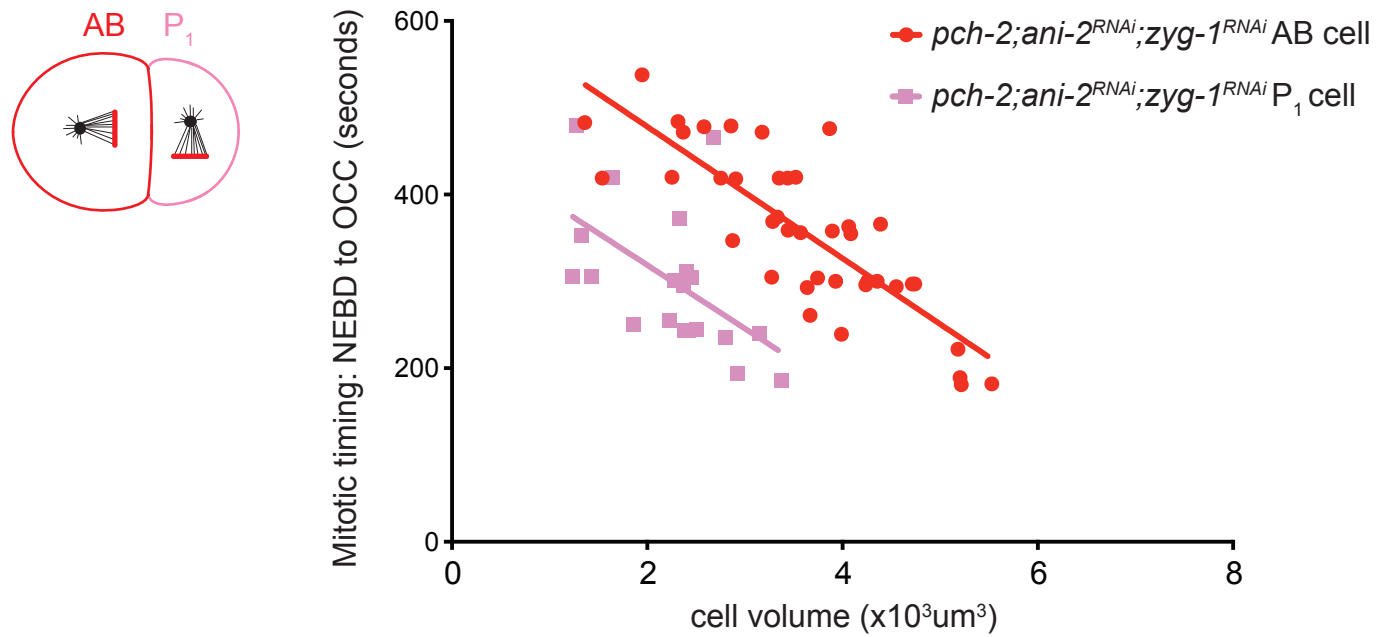
B



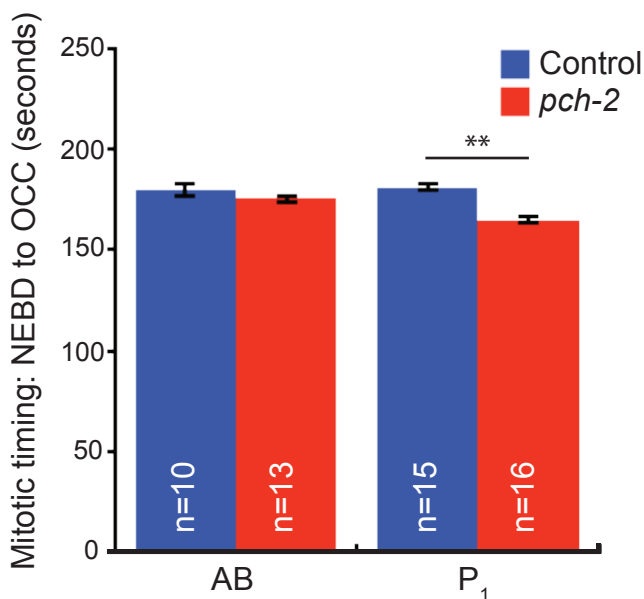
A

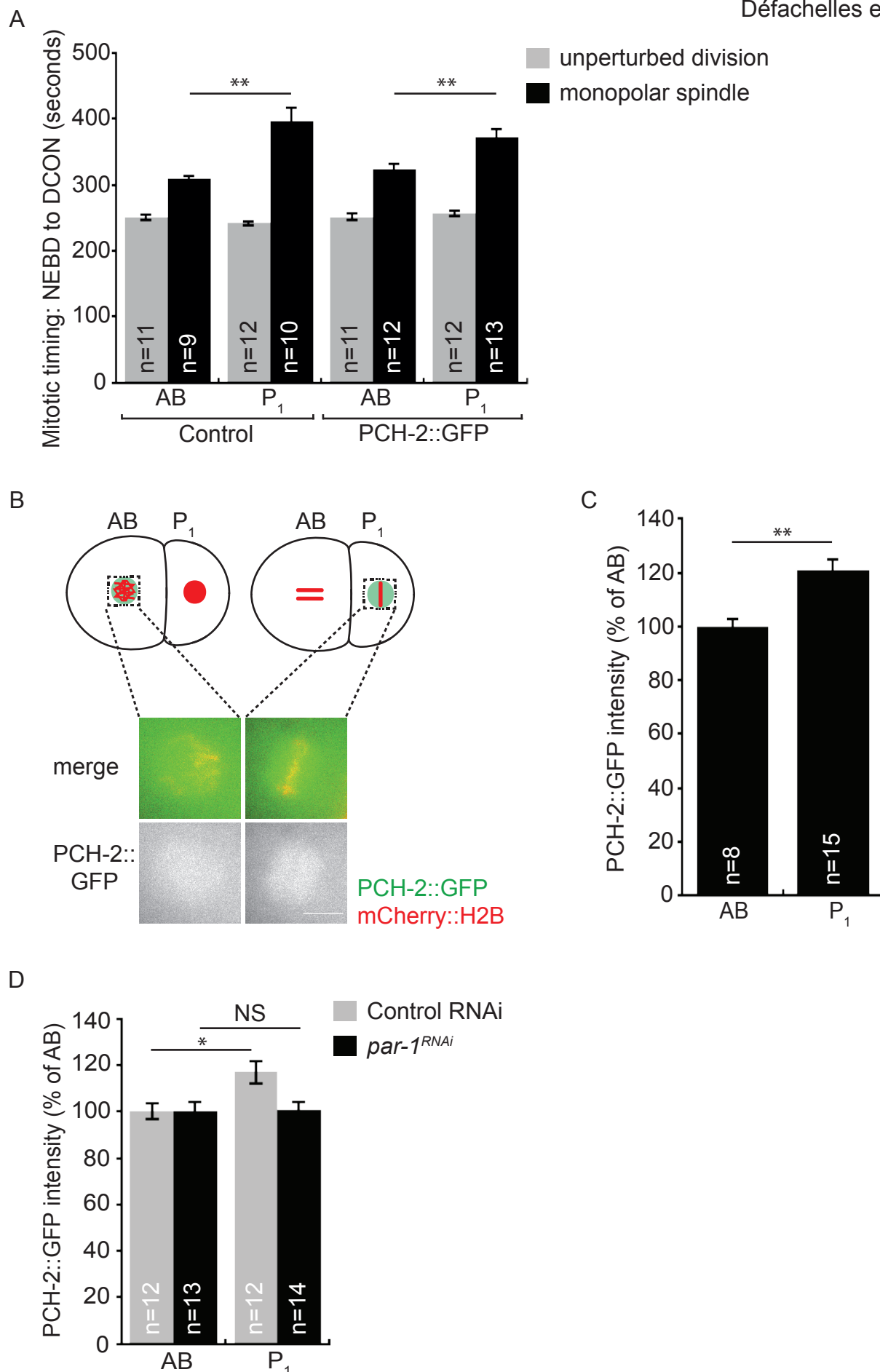


B

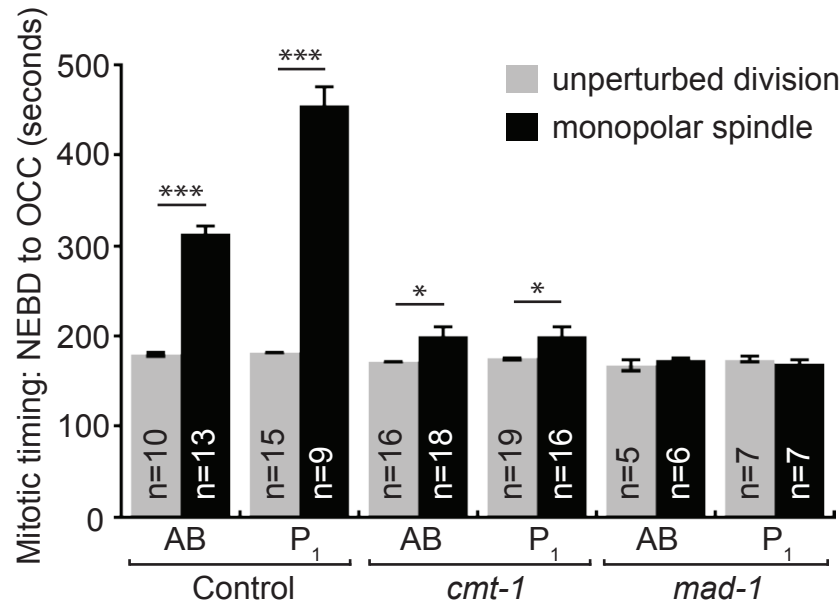


C

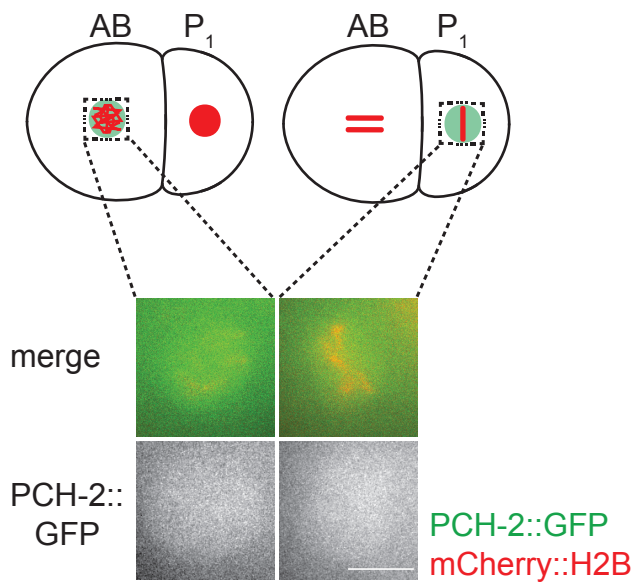




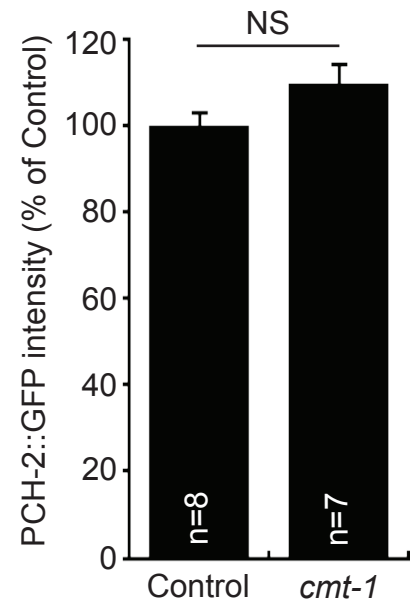
A



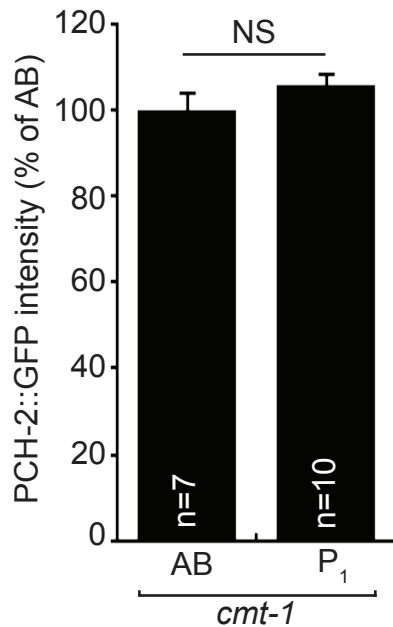
B

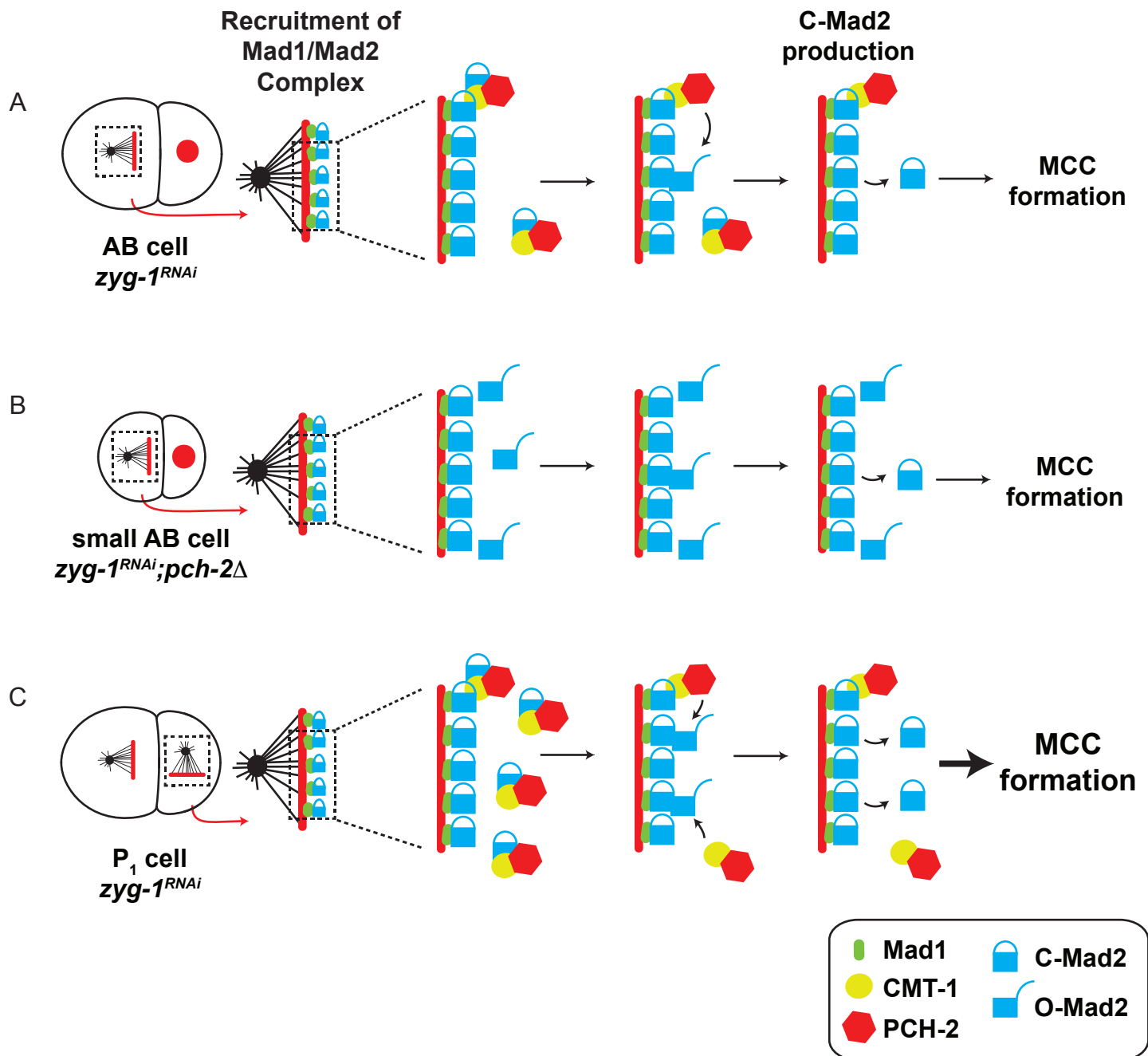


C



D





Strain	Genotype
OD56	<i>unc-119(ed3) III; ltIs37 [pAA64; Ppie-1::mCherry::his-58; unc-119 (+)] IV</i>
OD95	<i>unc-119(ed3) III; ltIs37 [pAA64; Ppie-1::mCherry::his-58; unc-119 (+)] IV; ltIs38 [pAA1; Ppie-1::GFP::PH(PLC1delta1); unc-119(+)]</i>
BHL575	<i>pch-2(tm1458) II; unc-119(ed3) III; ltIs37 [pAA64; Ppie-1::mCherry::his-58; unc-119 (+)] IV; ltIs38 [pAA1; Ppie-1::GFP::PH(PLC1delta1); unc-119(+)]</i>
BHL596	<i>unc-119(ed3) III; ltIs37 [pAA64; Ppie-1::mCherry::his-58; unc-119 (+)] IV; ltIs38 [pAA1; Ppie-1::GFP::PH(PLC1delta1); unc-119(+)]; mdf-1(av19) V</i>
BHL600	<i>unc-119(ed3) III; ltIs37 [pAA64; Ppie-1::mCherry::his-58; unc-119 (+)] IV; ltIs52 [pOD379; Ppie-1::GFP::MDF-2; unc-119 (+)]</i>
BHL604	<i>pch-2(tm1458) II; unc-119(ed3) III; ltIs37 [pAA64; Ppie-1::mCherry::his-58; unc-119 (+)] IV; ltIs52 [pOD379; Ppie-1::GFP::MDF-2; unc-119 (+)]</i>
BHL608	<i>cmt-1(ok2879) I; unc-119(ed3) III; ltIs37 [pAA64; Ppie-1::mCherry::his-58; unc-119 (+)] IV; ltIs38 [pAA1; Ppie-1::GFP::PH(PLC1delta1); unc-119(+)]</i>
BHL664	<i>Ppch-2::pch-2::GFP-3XFLAG (blt4 [pCN94]) II; unc-119(ed3) III; ltIs37 [pAA64; Ppie-1::mCherry::his-58; unc-119 (+)] IV</i>
BHL883	<i>san-1/mdf-3 (ok1580) I; pch-2(tm1458) II; unc-119(ed3) III; ltIs37 [pAA64; Ppie-1::mCherry::his-58; unc-119 (+)] IV; ltIs38 [pAA1; Ppie-1::GFP::PH(PLC1delta1); unc-119(+)]</i>
BHL887	<i>cmt-1(ok2879) I; pch-2::GFP-3XFLAG (blt4 [pCN94]) II; unc-119(ed3) III; ltIs44[pAA173; pPie-1::mCherry::PH(PLC1delta1); unc-119(+)]; ltIs37 [pAA64; Ppie-1::mCherry::his-58; unc-119 (+)] IV</i>
BHL888	<i>unc-119(ed3) III; ltIs44 [pAA173; pPie-1::mCherry::PH(PLC1delta1); unc-119(+)]; ltIs52 [pOD379; Ppie-1::GFP::mdf-2; unc-119 (+)]; ltIs37 [pAA64; Ppie-1::mCherry::his-58; unc-119 (+)] IV</i>
BHL889	<i>pch-2(tm1458) II; unc-119(ed3) III; ltIs44 [pAA173; pPie-1::mCherry::PH(PLC1delta1); unc-119(+)]; ltIs52 [pOD379; Ppie-1::GFP::mdf-2; unc-119 (+)]; ltIs37 [pAA64; Ppie-1::mCherry::his-58; unc-119 (+)] IV</i>
BHL891	<i>unc-119(ed3) III; ltIs37 [pAA64; Ppie-1::mCherry::his-58; unc-119 (+)] IV; ltIs24[pAZ132; pPie-1::GFP::tba-2; unc-119(+)]</i>
BHL892	<i>pch-2 (tm1458) II; unc-119(ed3) III; ltIs37 [pAA64; Ppie-1::mCherry::his-58; unc-119 (+)] IV; ltIs24 [pAZ132; pPie-1::GFP::tba-2; unc-119(+)]</i>
BHL893	<i>san-1/mdf-3 (ok1580) I; unc-119(ed3) III; ltIs37 [pAA64; Ppie-1::mCherry::his-58; unc-119 (+)] IV; ltIs38 [pAA1; Ppie-1::GFP::PH(PLC1delta1); unc-119(+)]</i>
BHL904	<i>Ppch-2::pch-2::GFP-3XFLAG (blt4 [pCN94]) II; unc-119(ed3) III; ltIs44[pAA173; pPie-1::mCherry::PH(PLC1delta1); unc-119(+)]; ltIs37 [pAA64; Ppie-1::mCherry::his-58; unc-119 (+)] IV</i>
GAL5	<i>san-1/mdf-3 (mat5) I; unc-119(ed3) III; ruls57[Ppie-1::GFP::tubulin + unc-119(+)]; ltIs37[pie-1p::mCherry::his-58 (pAA64) + unc-119(+)] IV</i>

